

Acoustic Valley-Hall Edge States in phononic elastic waveguides

Ting-Wei Liu and Fabio Semperlotti*

*Ray W. Herrick Laboratories, School of Mechanical Engineering,
Purdue University, West Lafayette, Indiana 47907, USA.*

(Dated: December 14, 2024)

This study presents the occurrence of acoustic topological edge states in a 2D phononic elastic waveguide due to a phenomenon that is the acoustic analogue of the quantum valley Hall effect. We show that the topological phase transition takes place between two lattices in which the space inversion symmetry is broken due to the application of an antisymmetric strain field. This condition leads to the formation of gapless edge states at the domain walls, as also further illustrated by the analysis of the bulk-edge correspondence and of the associated topological invariants. Although time reversal symmetry is still intact in these systems, the edge states are topologically protected when inter-valley mixing is either weak or negligible. Interestingly, topological edge states can also be triggered at the boundary of a single domain if boundary conditions are properly selected. We also show that the static modulation of the strain field allows tuning the response of the material between the different supported edge states.

During the past few years, topological acoustics has rapidly emerged as a new and fascinating branch of physical acoustics. Following the groundbreaking research in solid state physics, which showed the existence of topological states of matter [1, 2], researchers have been able to formulate the acoustic analogue of selected mechanisms. In solid state physics, one of the first implementations of topological materials was based on the use of the Quantum Hall Effect (QHE) which leveraged the use of an external magnetic field to break time-reversal symmetry (TRS). While in electronic systems the application of a magnetic field is a rather simple way to achieve TRS breaking, in acoustics the process is more complicated due to the intrinsic reciprocal nature of acoustic waves. The first few attempts at breaking TRS in an acoustical system exploited the use of rotating inclusions (such as spinning rotors [3, 4] or fluid flows [5–7]). These designs were able to break reciprocity and to induce one-way propagating edge states, however they were often impractical to fabricate and required an external active input and/or control. Later versions of topological acoustic systems were developed based on the acoustic analogue of the Quantum Spin Hall Effect (QSHE) [8–10] which, contrarily to the QHE, requires intact TRS. By leveraging the coupling between modes associated with two coincident Dirac cones, researchers were able to create the acoustic analogue of the electronic spin-orbit coupling, therefore achieving unidirectional edge states topologically protected from back-scattering.

During the last decade, several studies have investigated the design of topological materials based on broken space-inversion symmetry (SIS). For electronic materials, SIS was broken using different methodologies including graphene-like lattices with staggered sublattice potentials [11–15], strained graphene [16], and multi-layered graphene under electric fields [17–21]. The effect of the asymmetry is that of opening a gap at the original Dirac cone associated with the hexagonal lattice in which edge

states are now supported. Note that these edge states cannot be explained by the previously mentioned QHE or QSHE mechanisms. In fact, when only SIS is broken the lattice still possesses a trivial topology within the context of QHE [1, 22, 23] and QSHE [24, 25]. However, due to the large separation in \mathbf{k} -space of the two valleys (i.e. the Dirac points occurring at the corners of the Brillouin zone, the \mathbf{K} and \mathbf{K}' symmetry points), valley-dependent topological invariants can be defined and used to classify the topological states of the different lattices. This approach, usually referred to as quantum valley Hall effect (QVHE), was recently investigated for application to acoustic waveguides [26, 27].

In the present study, we consider the dispersion and propagation behavior of an elastic phononic waveguide assembled from a truss-like unit cell having hexagonal D_{6h} symmetry (Fig. 1(a)). The fundamental lattice structure clearly exhibits SIS with inversion axes located at the nodal points. The lattice is then deformed by applying an internal pressure δp that lowers the symmetry to D_{3h} . The equivalent force produced by the δp is locally normal to the individual truss element as shown in Fig. 1(d). The application of either a positive or a negative pressure δp results in two different deformed states of the lattice that for simplicity we label as α - and β -states (Fig. 1(b),(c)), respectively. In these states, the SIS is clearly broken.

We will show in the following that 1) the evolution from α - to β -state (and viceversa) is accompanied by a topological phase transition, and that 2) when a phononic system is obtained by assembling the two phases, an edge state is supported along the domain wall (i.e. the interface between the α - and β -state). We will also show that these edge states can be created and modulated at the boundary of a single lattice by selecting proper boundary conditions and by tuning the internal pressure. We will use a combination of theoretical and numerical tools to show that the deformed lattices belong to different topo-

logical phases and that their combination induce a phase transition that supports edge states. In particular, we started the analysis building a model of the periodic lattice. Consider the truss-like phononic crystal with hexagonal lattice structure. The individual trusses are assumed made out of aluminum, and having width $w = 0.1a$, and thickness $t = 0.05a$ where a is the lattice constant. By applying the Bloch theorem on the unit cell, both the phononic band structure and the eigenstates can be calculated. This is considered as the reference lattice and it clearly exhibits intact SIS.

As previously mentioned, the SIS of the reference lattice can be broken by introducing an external perturbation resulting in a local strain field. At this stage, we are not concerned with the details of the local perturbation that, in practical applications, could be implemented in different forms (e.g. mechanical or thermal loads, active materials, etc.). For the purpose of this study, we assume that the perturbation is applied in the form of an isostatic pressure δp applied on the side walls of the triangular subcell and following a 3-fold rotation symmetry. In such a scheme, the triangular subcells composing the hexagonal unit cell alternate states of positive and negative pressure δp . Depending if a positive or a negative δp is applied to the fundamental triangular subcell, either the α - or β -states are obtained. It is easy to see that the states α and β are inverted images of each other, and they turn into each other as δp switches sign.

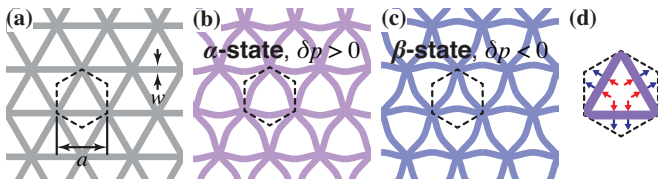


FIG. 1. (Color online) Schematic illustration of the lattice geometry. (a) The reference crystal (unstrained) consisting of an aluminum truss-like hexagonal lattice having SIS. The dashed black line indicates the primitive Wigner-Seitz cell. (b, c) The deformed α - and β -lattices obtained upon application of internal wall pressure. In both configurations SIS is broken. (d) The red and blue arrows show the direction of the positive and negative δp , respectively.

To have observable symmetry breaking, geometric nonlinearities due to large deflections must be considered. Note that the system configuration at hand allows obtaining large deflections still associated with infinitesimal strains, so that the constitutive relations are still linear. Under this condition, the analysis can be divided in two parts: 1) a nonlinear static analysis to calculate the state of displacement \mathbf{u}_0 , stress \mathbf{s}_0 , and strain ϵ_0 induced by the applied pressure load, and 2) a linear wave propagation analysis around the pre-stressed equilibrium state.

Assuming that the pre-stressed state is available from a previously performed static calculation, the dynamic

response can be studied as linear small oscillations $\mathbf{u}'e^{i\omega t}$ around the new static equilibrium \mathbf{u}_0 , and the total displacement can be later expressed as $\mathbf{u}(\mathbf{t}) = \mathbf{u}_0 + \mathbf{u}'e^{i\omega t}$. Under these conditions the linearized wave equation is given by

$$\rho \frac{\partial^2 \mathbf{u}}{\partial t^2} = -\nabla \cdot \mathbf{P}, \quad (1)$$

which is readily rewritten as:

$$-\rho \omega^2 \mathbf{u}' = -\nabla \cdot \mathbf{P}, \quad (2)$$

where ρ is the mass density, $\mathbf{P} = (\nabla \mathbf{u} + \mathbf{I})\mathbf{s}$ is the first Piola-Kirchhoff stress tensor, \mathbf{s} is the second Piola-Kirchhoff stress tensor with $\mathbf{s} = \mathbf{s}_0 + \mathbf{C} : (\epsilon - \epsilon_0)$, where \mathbf{C} is a 4th order elasticity tensor, and \mathbf{s}_0 and ϵ_0 are the initial stress and strain, respectively. Solving the \mathbf{k} -dependent Bloch eigenvalue problem yields the phononic band structure and the eigenstates. The above described model was assembled and solved using the commercial finite element software COMSOL Multiphysics.

The resulting phononic band structure, limited to the flexural modes, is shown in Fig. 2. The frequency is normalized by the bulk shear wave speed in aluminum, $c = 3099\text{m/s}$, over the lattice constant a . Note that the current system is effectively a flat waveguide that admits Lamb guided modes. However, in the following, we concentrate only on flexural A (antisymmetric) modes that are those more naturally excited in plate-like structures under external excitation.

Fig. 2 (a) and (b) show the band structures of the lattice with $\delta p = 0$ (intact SIS) and $\delta p = 20\text{ MPa}$ (broken SIS), respectively. The value of the pressure perturbation was chosen according to the previously mentioned criterion which requires large deflections but linear strains. Note that the two lattices in states α and β have identical band structure (Fig. 2 (b)) since they are simply spatially inverted versions of each other and with intact TRS. Similarly, comparing the valley properties at the symmetry points $\mathbf{K} = \frac{4\pi}{3a}\hat{x}$ and $\mathbf{K}' = -\mathbf{K}$ within the same lattice (either in α - or β -state) is equivalent to comparing properties of the α - and β -lattices at the same symmetry point.

The analysis of the dispersion properties in Fig. 2 (a) reveals the existence of a degeneracy at the \mathbf{K} point from which locally linear dispersion curves emanate. This dispersion structure, known as the Dirac cone (DC), is fairly common in hexagonal lattices and it was observed before in other material systems (e.g. graphene) [28, 29]. The DC is protected by the lattice configuration however, when SIS is broken (Fig. 2 (b)), the degeneracy is lifted and the initially degenerate modes can separate and give rise to a local bandgap. It is the adiabatic evolution of this specific dispersion structure under small perturbations that enables the generation of topological edge

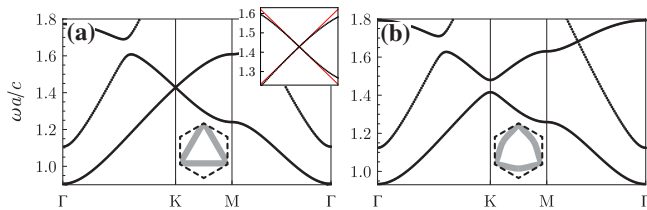


FIG. 2. Phononic band structure of (a) the undeformed lattice (shown in Fig. 1 (a)), and of (b) the α - (or β -) lattice (shown in Fig. 1 (b) and (c)). An incomplete bandgap opens up at the original Dirac point as SIS is broken. The inset in (a) shows the comparison between the numerical dispersion data (black dots) and the dispersion predicted by the $\mathbf{k} \cdot \mathbf{p}$ method (red lines) near the Dirac point.

modes. In particular, we will show that the dispersion at the \mathbf{K} (or, equivalently, the \mathbf{K}') point in either the reference or the perturbed configuration can be mapped into a massless or a massive Dirac equation, respectively. Before proceeding, we should also note that the current configuration produces an incomplete bandgap (Fig. 2b). In principle, a complete bandgap could be obtained by optimization of the lattice geometric parameters [9], however we will show that the valley-dependent design is fairly robust and does not impose strict requirements on the nature of the bandgap.

It was established above that the process of lifting the degeneracy and opening the bandgap is connected to the applied pressure perturbation within the cell. Fig. 3 (a) and (b) show the evolution of the gap bounds as well as of the width of the gap as a function of the applied pressure δp . An average upward shift of the frequency is observable in the gap bounds as $|\delta p|$ increases. This behavior is directly related to the stress stiffening effect produced by the geometrically nonlinear deformation of the cell. The analysis of the gap width indicates that the gap vanishes and reopens as δp crosses zero, therefore suggesting a topological phase transition in the δp -space.

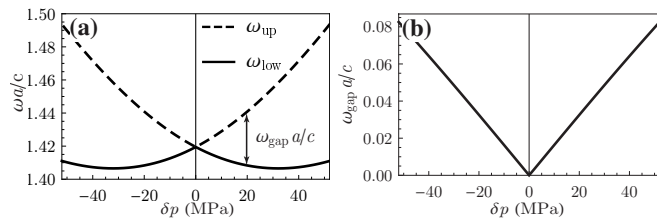


FIG. 3. Effect of the applied perturbation δp on (a) the evolution of the upper and lower bounds of the bandgap, and (b) the gap width. The gap's bounds tend to shift upward as $|\delta p|$ increases, however the gap width varies linear with δp .

The evolution of the bandgap as a function of δp suggests that, a lattice obtained by connecting α and β domains should experience a topological phase transition associated with a vanishing gap occurring exactly at the

domain wall (DW). The topological nature of this transition can be characterized using a topological invariant, that is the Chern number C_n (module 2π). The parameter C_n is obtained by integrating the Berry curvature $\Omega_n(\mathbf{k}) = \nabla_{\mathbf{k}} \times \langle \mathbf{u}_n(\mathbf{k}) | i \nabla_{\mathbf{k}} | \mathbf{u}_n(\mathbf{k}) \rangle \cdot \hat{\mathbf{z}}$ of the n^{th} mode throughout the first Brillouin zone. For our system, C_n is expected to be zero due to an odd distribution of the Berry curvature in \mathbf{k} -space, which should be expected given TRS is preserved [1, 22, 23]. It follows that these lattices are classified as trivially gapped materials (i.e. they have trivial topology) in the context of QHE systems. Nevertheless, for small SIS breaking, the Berry curvature is highly localized at the valleys (i.e. around the \mathbf{K} and \mathbf{K}' symmetry points), and the local integral of the Berry curvature converges quickly to a non-zero quantized value [11, 21]. This local integral is often referred to as the valley Chern number C_v of the n^{th} band and it is defined as

$$2\pi C_v = \int \Omega_n(\mathbf{k}) d^2\mathbf{k} \quad (3)$$

where the integral bounds extend to a local area around the valley. The right hand side of this equation is also referred to as topological charge. Previous studies in electronic systems [13] have shown that this quantized value has important implications because it characterizes the bulk-edge correspondence. This property is of particular importance for our system because the difference between the valley Chern numbers of the upper (or lower) bands of two adjacent lattices indicates the number of gapless edge states expected at the DW. Fig. 4(a) shows the calculated dispersion surfaces of the flexural modes of the α -lattice near the valley \mathbf{K} .

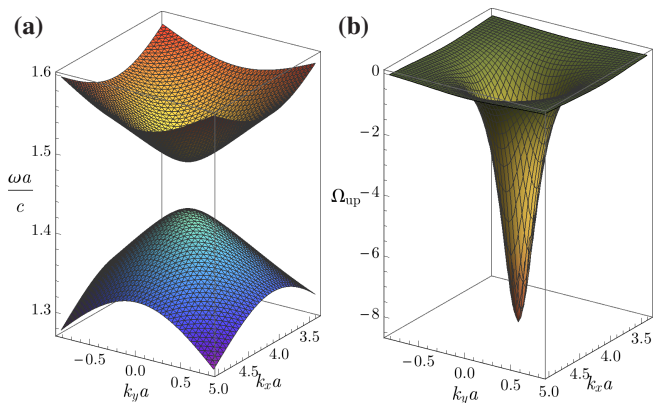


FIG. 4. (Color online) (a) The dispersion of the flexural A modes of the α -lattice near the \mathbf{K} valley. (b) The corresponding Berry curvature of the upper mode (the lower mode carries an equivalent Berry curvature of opposite sign).

Fig. 4(b) shows the Berry curvature corresponding to the upper mode (clearly the lower band carries Berry curvature of opposite sign). Numerical integration of the Berry curvature around the \mathbf{K} and \mathbf{K}' symmetry points

shows that each valley of either the α - or β -lattices carries a topological charge of magnitude π . The two lattices clearly exhibit Berry curvatures of opposite signs. It follows that, for the upper mode of the valley \mathbf{K} , the valley Chern numbers are $-\frac{1}{2}$ for the α -lattice and $+\frac{1}{2}$ for the β -lattice. The difference between these two indexes indicates the number of gapless edge states expected due to the topological transition at the interface. In our case, this difference $|C_v^\alpha - C_v^\beta| = 1$ therefore indicating the existence of a gapless edge state at the DW between the α - and β -lattices.

There are two possible configurations of the DWs between the α - and β -lattices, that is α on top ($+y$) of β or viceversa (see Fig. 5 (a) and (b)). Note that these two configurations are not equivalent, and are dominated by a mirror symmetry with respect to DW1 and DW2, respectively. As a direct consequence of the mirror symmetry, the edge states propagating along the domain walls can be either symmetric or anti-symmetric (with respect to the DW interface). This symmetry was exploited in order to reduce the size of the finite element model. In particular, we built an α -state superlattice ribbon made of 37 triangular subcells stacked along the y -direction (see the red part in Fig. 5 (a)) and amounting to a length of about $64a$. Then, either symmetric or anti-symmetric boundary conditions along DW1 or DW2 were applied to simulate the presence of the β -state ribbon. The model was solved to get the solution of the Bloch eigenvalue problem. Results show that the edge state at DW1 is anti-symmetric, while at DW2 it is symmetric. Fig. 5 (c) shows the dispersion relation of such a ribbon structure.

The x projection of the wavevector at the valley $\mathbf{K}' = -\frac{4\pi}{3a}\hat{x}$ on the irreducible Brillouin zone is $k_x a = \frac{2\pi}{3}$. Due to symmetry, the projection of the valley \mathbf{K} belongs to the other half of the first Brillouin zone (not shown) which is simply a mirror image (with respect to $k_x a = \pi$). The colorbar denotes the y -position of the centroid of the superlattice weighted by the strain energy density. The blue color indicates edge states at DW1 while the red color indicates edge states at DW2. The two modes have equal and opposite group velocities but since they are supported by the two different edges of the lattice they cannot couple. In addition, if inter-valley mixing is neglected (due to large separation in \mathbf{k} -space between the \mathbf{K} and \mathbf{K}' points), these edge states are immune to back-scattering. Note that this assumption is well verified in the absence of short range disorder. We highlight that this dynamic behavior is effectively equivalent to the QSHE in topological insulators if the spin index is replaced by the valley index, as shown in Fig. 5 (b). In order to further confirm the characteristics of these edge modes, we performed full field numerical simulations. In particular, we simulated the steady-state response of two different DW shapes (i.e. straight and arbitrary) when excited by a point excitation. Low-reflecting boundaries

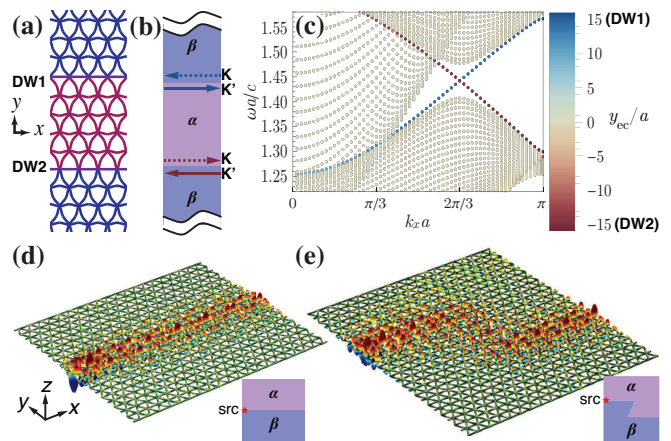


FIG. 5. (Color online) (a) Lattice structure and (b) schematic illustration of the two possible DW configurations based on the α - and β -lattices. Each DW allows propagation of an edge state for each valley index. (c) Dispersion curves in a superlattice ribbon containing 37 triangular subcells of α -lattices stacked along the y -direction, with symmetric boundary conditions. The valley $\mathbf{K}' = -\frac{4\pi}{3a}\hat{x}$ projects on $k_x a = \frac{2\pi}{3}$ in the irreducible Brillouin zone. The colorbar denotes the y -position of the centroid of the superlattice weighted by the strain energy density: modes in blue color are edge states at DW1, while modes in red indicates edge states at DW2. (d, e) Full field simulations of the edge states along a straight and an arbitrary-shaped DW. The modes were excited by a harmonic point source. Low reflecting boundaries were used all around the model to suppress the effect of reflections.

were used all around the model to suppress the effect of reflections. In both cases, results show that the edge states are well concentrated near the DWs and are guided along the wall itself (Fig. 5 (d),(e)).

Although the band structure and the valley Chern number were accurately calculated via a numerical approach, it is still useful to introduce a semi-analytical model to further analyze the effects of SIS-breaking on the phononic waveguide.

Starting from the (undeformed) reference lattice configuration which still preserves SIS, the $\mathbf{k} \cdot \mathbf{p}$ perturbation approach [30] can be used to show that the linear dispersions at the valleys can be mapped to a massless Dirac equation. The method allows obtaining approximate solutions to the governing equations by using the degenerate modes as fundamental basis of an expansion process. In this method, the origin of the \mathbf{k} -axes is shifted to the degeneracy by letting $\mathbf{q} \equiv \mathbf{k} - \mathbf{K}$ (or $\mathbf{k} - \mathbf{K}'$) and $\nu \equiv \omega - \omega_0$. Hence, the problem of determining the dispersion relations $\nu - \mathbf{q}$ is cast in the form of a 2×2 eigenvalue problem associated to the following Hamiltonian

$$\mathcal{H}(\mathbf{q}) = v_g \mathbf{q} \cdot \vec{\sigma}, \quad (4)$$

where v_g is the group velocity, and $\vec{\sigma} \equiv (\sigma_1 \sigma_2 \sigma_3)$ are Pauli matrices. Eq. (4) maps to the massless Dirac

equation associated with locally linear dispersion. By extracting the eigenstates from the previous simulations, we can numerically confirm that the group velocity $v_g = \pm 0.138c$ obtained from the $\mathbf{k}\cdot\mathbf{p}$ method matches well with the tangent slopes of the exact dispersion data obtained from numerical calculations (cf. inset in Fig. 2 (a)).

When SIS is broken by the application of a pressure perturbation δp , the degeneracy at \mathbf{K} (or \mathbf{K}') is lifted, the modes become non-degenerate, and a gap opens up. It is well-known that breaking SIS introduces a σ_3 -component into the Hamiltonian that can be expressed as [1, 22],

$$\mathcal{H}(\mathbf{q}) = v_g \mathbf{q} \cdot \vec{\sigma} + m \sigma_3, \quad (5)$$

Eq. (5) represents the Hamiltonian of a massive Dirac equation which we show applies also to our specific lattice structure. Since the SIS-breaking perturbation is small, it can be expressed as a perturbation of the massless Hamiltonian,

$$\mathcal{H}(\mathbf{q}) = v_g \mathbf{q} \cdot \vec{\sigma} + \vec{m} \cdot \vec{\sigma}, \quad (6)$$

where we assumed a general perturbation that potentially contains all the four Pauli matrix components ($\vec{\sigma} = [\sigma_1, \sigma_2, \sigma_3]$) as well as the identity matrix σ_0 . At the \mathbf{K} (or \mathbf{K}') point ($\mathbf{q} = \mathbf{0}$), the Hamiltonian reduces to

$$\mathcal{H}(\mathbf{0}) = \vec{m} \cdot \vec{\sigma}. \quad (7)$$

Let $\mathbf{u}_{1,2}^d$ be the two degenerate modes of the undeformed lattice and $\mathbf{u}_{1,2}^n$ be the two non-degenerate modes of the deformed lattice, at $\mathbf{q} = \mathbf{0}$. These modes are available from the numerical calculation of the band structure. By performing the inner product

$$I_{ij} \equiv \int_{\text{unit cell}} \mathbf{u}_i^d \cdot \mathbf{u}_j^n d^3 \mathbf{r}, \quad (8)$$

it is seen that matrix I is diagonal (or anti-diagonal, depending on the numbering of the modes), which implies that $\mathcal{H}(\mathbf{0}) = \vec{m} \cdot \vec{\sigma}$ is also diagonal. This means that the perturbation term can only contain σ_0 and σ_3 components, at most. In particular, the splitting of the eigenfrequencies is connected to the σ_3 component while the average upward shift of the bands (as a function of δp) is connected to the σ_0 component. Note that the σ_0 term does not affect either the eigenvectors or the topological properties, hence it can be omitted in the Hamiltonian. The above arguments confirm that the Bloch eigenvalue problem of the SIS-broken lattice can be mapped to the massive Dirac equation (Eq. (5)).

The bulk dispersion is then given by $\nu(\mathbf{q}) = \pm \sqrt{|v_g \mathbf{q}|^2 + m^2}$ with a gap equal to $2|m|$. From the numerical results in Fig. 3 (b) we find that $|m| = 0.000795 \text{MPa}^{-1} \delta p$, where δp is expressed in MPa.

The corresponding Berry curvature, associated with the evolution of the eigenvectors in \mathbf{k} -space, has a distribution sharply peaked at the two Dirac points,

$$\Omega(\mathbf{q}) = \frac{1}{2} \tau m v_g^2 (|\mathbf{q}|^2 v_g^2 + m^2)^{-\frac{3}{2}}, \quad (9)$$

where $\tau = \pm$ allows simple labeling of the two valleys \mathbf{K} and \mathbf{K}' . Integrating Eq. (9) on a small area around the symmetry points gives the valley Chern number $C_v = \frac{1}{2} \tau \text{sgn}(m)$. Under TRS, $m_{\mathbf{K}} = m_{\mathbf{K}'}$ for either a lattice α or β , and $m^\alpha = m^\beta$ at the same valley. Thus $|C_v^\alpha - C_v^\beta| = 1$ is always true. Hence, we can conclude that there is one gapless edge state living on the DW connecting the two lattice α and β .

Here above, we presented the characterization of the dynamic response of the domain wall between topologically different lattices. In the following, we address the case where edge states occur at the boundary of an individual lattice with broken SIS. In this case, the topological phase transition is not due to the existence of a domain wall but, instead, to the presence of the boundary. The two specific boundary conditions under evaluation are traction-free and fixed. Each boundary condition can be applied on the top ($+y$) and bottom ($-y$) boundaries of the ribbon (either in α - or β -state), hence resulting in a total of 8 possible configurations (Fig. 6 (a)-(d)). However, since the α - and β -lattices are inverted images of each other, a given boundary condition on the edge of an α -ribbon corresponds to the inverted image of the same boundary condition on the opposite edge of a β -ribbon (see, for example, in Fig. 6 the pairs (a)/(c) and (b)/(d)). Note that, although they have the same edge dispersion, the valley indices interchange.

The boundary conditions can be classified into four groups yielding different dispersion. Not all the four groups of boundary conditions yield edge modes. Only the two edges of the ribbon β in Fig. 6 (a) (or the edges of ribbon α in Fig. 6 (c)) have propagating edge states, as shown in Fig. 6 (e). The other two groups (Fig. 6 (b) and (d)) do not support edge states (Fig. 6 (f)). In this last case, the edge mode (blue color) visible in the dispersion belongs to the bulk and can be neglected. An interpretation of this behavior is provided here below.

Recall that DW1 supports an anti-symmetric edge state. Anti-symmetry requires $\mathbf{u} \cdot \mathbf{t} = 0$ on the interface, where \mathbf{t} is any tangent vector to the interface, therefore having the direction of either $\hat{\mathbf{x}}$ or $\hat{\mathbf{z}}$. To satisfy the anti-symmetry condition u_x and u_z must be zero, while the u_y component are non-zero. The A modes, under consideration in this study, exhibit particle displacement mostly dominated by the u_z component. When a fixed boundary condition is imposed along the edge, the particle displacement \mathbf{u} is set to zero therefore resembling the behavior of the anti-symmetric interface. On the other hand, DW2 supports symmetric edge states. At the interface we have $\mathbf{u} \cdot \hat{\mathbf{y}} = 0$, without restriction on u_z . Similarly to the discussion above, the traction free boundary condition will allow u_z therefore behaving more closely to a symmetric interface.

As a result, each of the fixed boundaries in Fig. 6 (a) and (c) is dynamically equivalent to half of the DW1. This boundary configuration supports edge states simi-

lar to those observed along DW1, but without connecting the two continuous bulk bands (i.e. the red modes in Fig. 6 (e)). Similarly, each of the free boundaries in Fig. 6 (a) and (c) supports an edge state that does not cross the bandgap. On the contrary, the other two groups of boundary conditions (Fig. 6 (b) and (d)) break the similarity with the DWs, therefore the edge states are strongly suppressed.

Full field numerical simulations confirmed this behavior and showed that edge states can be excited on the fixed edge on the top of an α -ribbon, but it cannot be excited under equivalent conditions in a β -ribbon (see Fig. 7 (a) and (b)). These two conditions correspond to the fixed edges in Fig. 6 (c) and (b), respectively.

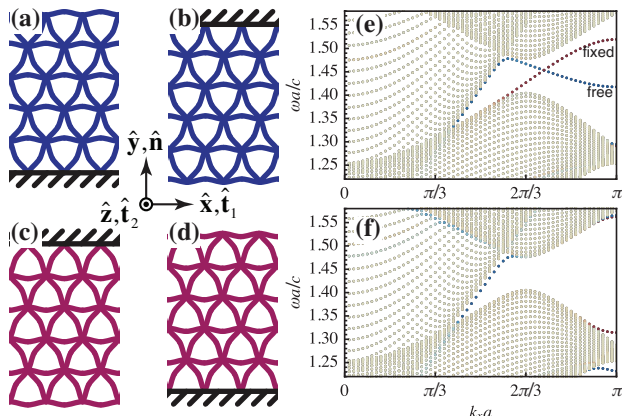


FIG. 6. (Color online) (a-d) Schematic of the eight different boundary configurations involving fixed and traction free conditions on the top (+y) or bottom (-y) boundaries of the α - or β -ribbons. The configurations (a) and (c) yield two edge states associated with the dispersion shown in (e). The two boundary conditions in (b) and (d) do not yield topological edge states, as shown in (f).

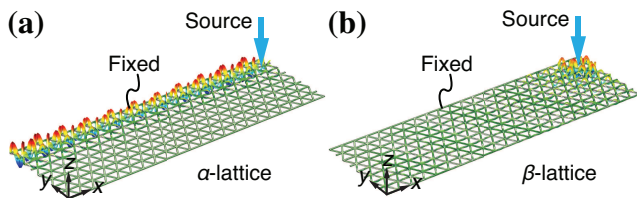


FIG. 7. (Color online) Full field numerical simulations showing that (a) edge states can be excited on the fixed edge on the top of an α -ribbon, while (b) they cannot be excited at the same position in a β -ribbon.

Yao et al. [13] showed that on a graphene system with staggered sublattice potential, the edge states dispersion can be controlled by the on-site energy on the boundary cells. Similarly, in our system the phononic edge states dispersion can be manipulated by tuning the pressure of the outermost row of lattice. From the dispersion curve (Fig. 6 (e)), we observe that the edge state develops from

the bulk band near the valley and as k_x increases the edge state localizes more sharply on the edge. At $k_x a = \pi$, the energy is mostly confined in the outermost row of the lattice, therefore controlling the edge state requires tuning the outermost cell properties.

For our phononic waveguide, a general trend can be established observing that a positive pressure on the outer cells tends to increase the edge state frequency at $k_x a = \pi$, while a negative pressure tends to decrease it. This suggests that the edge state dispersion can be tailored by controlling the local pressure in the edge cells.

Numerical results in Fig. 8 show that a combination of boundary conditions and local pressure allows tuning the edge states to either a partially gapped band, a gapless band, or a flat mode. As an example, by setting the outer cell pressure to $\delta p_o = +2.5|\delta p|$ near the fixed edge (cf. Fig. 6 (c)) the dispersion curve of the edge state bends up towards the top bulk band (Fig. 8 (a)). Similarly, by setting the outer cell pressure to $\delta p_o = -2.5|\delta p|$ near the free edge (cf. Fig. 6 (a)) the dispersion curve bends down towards the bottom bulk band (Fig. 8 (b)). Flat bands can also be obtained (Fig. 8 (c) and (d)) by applying $\delta p_o = 2|\delta p|$ and $-2|\delta p|$ in the previous two cases, respectively. For the two cases supporting the gapless edge states crossing the gap, the pressure applied on the outer cells has different sign from the bulk lattice. This situation is somewhat equivalent to introducing a DW on the boundary and it results again in the occurrence of gapless edge states due to the contrast between bulk topological charges.

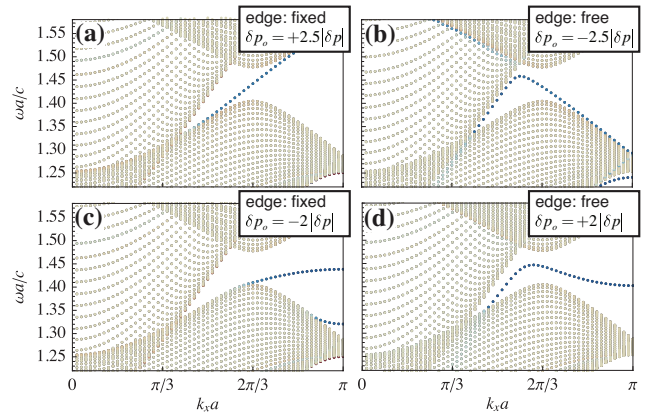


FIG. 8. (Color online) (a, b) Edge states at the fixed and free edge when the outer cell pressure is set to $\delta p_o = +2.5|\delta p|$ and $-2.5|\delta p|$, respectively. The edge states can be tuned to bend towards either the top or the bottom bulk bands. (c, d) Edge states at the fixed and free edge when the outer cell pressure is set to $\delta p_o = -2|\delta p|$ and $+2|\delta p|$, respectively. The edge states become flat bands.

These results deserve some additional discussion concerning the dispersion of the traction-free edge (Fig. 6 (f) and Fig. 8 (b), (d)). Note that the dispersion curves highlight the existence of a localized mode near the free

edge, which develops along the bulk band corresponding to the faster flexural branch. These parts have no topological significance and they are effectively surface-like waves with depth of the same order of the wavelength. To clarify this aspect further, consider a fin-like elastic waveguide with thickness t and width b . The fin can be thought as a continuum version of our phononic ribbon without the lattice structure. It is well-known that as $kb \gg 1$ the fundamental flexural mode develops into a surface wave (Fig. 9). This is similar to the S_0 and A_0 Lamb modes evolving into Rayleigh surface modes as $kt \rightarrow \infty$. Therefore, this edge mode has no topological significance as confirmed also by the zero Berry curvature being associated with the bulk bands (Fig. 2). Nevertheless, there is strong coupling between this mode and the topological edge states propagating along the same traction-free edge. To clarify the interaction between these two edge modes, we can plot again the results of Fig. 8 (b) with an emphasized nonlinear color scheme in Fig. 10. The gapless topological edge state and the non-topological edge state meet at the upper left of the cone, and there is a strong level repulsion indicating hybridization. When they enter the continuous bulk band of the other, they become strongly leaky due to the coupling with bulk modes.

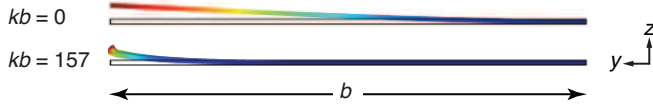


FIG. 9. (Color online) Cross-section view of the mode shapes of a fin-like elastic waveguide with thickness t and width b , at $kb = 0$ and $kb = 157$. The fundamental flexural mode develops into a surface wave as $kb \gg 1$.

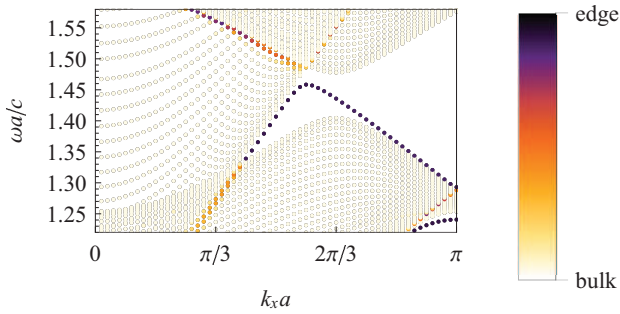


FIG. 10. (Color online) Results of Fig. 8 (b) plotted using a nonlinear color scheme based on the particle displacement. This plot clarifies the interaction between the two edge modes. The gapless topological edge state and the non-topological edge state meet at the upper left of the \mathbf{K} point, and experience a strong repulsion which indicates mode hybridization. When both modes enter the continuous bulk band, they become leaky waves due to the coupling with the bulk modes.

Finally we show that, despite TRS being still intact,

the two valley-dependent edge states can be excited individually when using a proper excitation. Since the two valley edge modes are largely separated in momentum space, the coupling between them is vanishingly small. This means that *valley-injection* can be achieved by using a source having stronger coupling with one of the two valleys. As an example, referring to the Bloch modes, two point sources distanced by a and having a phase difference $\pm 2\pi/3$ can selectively excite a specific mode. Full field numerical results are shown in Fig. 11 (a, b) for the DW and in Fig. 11 (c, d) for the fixed boundary. Again, low reflecting boundaries were used all around the model to suppress reflections.

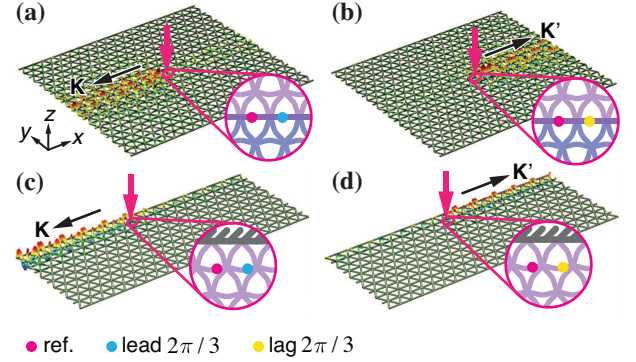


FIG. 11. Full field numerical simulations showing the ability to trigger a specific uni-directional edge state (either around the \mathbf{K} or \mathbf{K}' point) along either (a,b) a DW or (c,d) a fixed edge. The inset show that by selecting a proper two-point excitation with appropriate phase difference (matched to the targeted Bloch mode) accurate valley injection can be achieved.

In conclusion, we presented the design of topological elastic phononic waveguides based on the acoustic analog of the QVHE effect. The lattice structure exploited SIS-breaking while preserving TRS, hence resulting in a weak topological acoustic material. SIS breaking was induced by elastic deformation of the original lattice structure and topological transition was achieved by contrasting ribbons having different topological charges. This configuration could produce clear edge states at the domain wall interface. In a similar way, the proposed design was shown to be able to achieve topological edge states even in a single lattice configuration when in presence of specific boundary conditions. We showed that edge states could be efficiently tailored by tuning the pressure in the outermost edge cells. We also showed that, despite TRS being preserved, accurate valley injection could be effectively achieved by a two-point excitation therefore giving rise to uni-directional edge modes. In presence of smooth disorder, the inter-valley mixing is fairly weak which allows for back-scattering immune edge states.

The authors gratefully acknowledge the financial support of the Air Force Office of Scientific Research under

the grant YIP FA9550-15-1-0133.

* fsemperl@purdue.edu

- [1] M. Z. Hasan and C. L. Kane, *Rev. Mod. Phys.* **82**, 3045 (2010).
- [2] Y. Ren, Z. Qiao, and Q. Niu, *Rep. Prog. Phys.* **79**, 066501 (2016).
- [3] P. Wang, L. Lu, and K. Bertoldi, *Phys. Rev. Lett.* **115**, 104302 (2015).
- [4] L. M. Nasha, D. Kleckner, A. Reada, V. Vitellib, A. M. Turner, and W. T. M. Irvine, *Proc. Natl. Acad. Sci. U.S.A.* **112**, 14495 (2015).
- [5] A. B. Khanikaev, R. Fleury, S. H. Mousavi, and A. Alu, *Nat. Comms.* **6**, 8260 (2015).
- [6] Z. Yang, F. Gao, X. Shi, X. Lin, Z. Gao, Y. Chong, and B. Zhang, *Phys. Rev. Lett.* **114**, 114301 (2015).
- [7] Z.-G. Chen and Y. Wu, *Phys. Rev. Appl.* **5**, 054021 (2016).
- [8] R. Süssstrunk and S. D. Huber, *Science* **349**, 47 (2015).
- [9] S. H. Mousavi, A. B. Khanikaev, and Z. Wang, *Nat. Commun.* **6**, 8682 (2015).
- [10] C. He, X. Ni, H. Ge, X.-C. Sun, Y.-B. Chen, M.-H. Lu, X.-P. Liu, and Y.-F. Chen, *Nat. Phys.* **12**, 1124 (2016).
- [11] D. Xiao, W. Yao, and Q. Niu, *Phys. Rev. Lett.* **99**, 236809 (2007).
- [12] G. Semenoff, V. Semenoff, and F. Zhou, *Phys. Rev. Lett.* **101**, 087204 (2008).
- [13] W. Yao, S. A. Yang, and Q. Niu, *Phys. Rev. Lett.* **102**, 096801 (2009).
- [14] N. D. Drummond, V. Zolyomi, and V. I. Fal'ko, *Phys. Rev. B* **85**, 075423 (2012).
- [15] Y. Kim, K. Choi, and J. Ihm, *Phys. Rev. B* **89**, 085429 (2014).
- [16] F. Guinea, M. I. Katsnelson, and A. K. Geim, *Nat. Phys.* **6**, 30 (2009).
- [17] J. Jung, F. Zhang, Z. Qiao, and A. H. MacDonald, *Phys. Rev. B* **84**, 075418 (2011).
- [18] A. Vaezi, Y. Liang, D. H. Ngai, L. Yang, and E.-A. Kim, *Phys. Rev. X* **3**, 021018 (2013).
- [19] L. Ju, Z. Shi, N. Nair, Y. Lv, C. Jin, J. V. Jr, C. Ojeda-Aristizabal, H. A. Bechtel, M. C. Martin, A. Zettl, J. Analytis, and F. Wang, *Nature* **520**, 650 (2015).
- [20] F. Zhang, A. H. MacDonald, and E. J. Mele, *Proc. Natl. Acad. Sci. U.S.A.* **110**, 10546 (2013).
- [21] I. Martin, Y. Blanter, and A. F. Morpurgo, *Phys. Rev. Lett.* **100**, 036804 (2008).
- [22] S. Raghu and F. D. M. Haldane, *Phys. Rev. A* **78**, 033834 (2008).
- [23] T. Ochiai and M. Onoda, *Phys. Rev. B* **80**, 155103 (2009).
- [24] C. L. Kane and E. J. Mele, *Phys. Rev. Lett.* **95**, 146802 (2005).
- [25] D. N. Sheng, Z. Weng, L. Sheng, and F. D. M. Haldane, *Phys. Rev. Lett.* **97**, 036808 (2006).
- [26] J. Lu, C. Qiu, M. Ke, and Z. Liu, *Phys. Rev. Lett.* **116**, 093901 (2016).
- [27] J. Lu, C. Qiu, L. Ye, X. Fan, M. Ke, F. Zhang, and Z. Liu, *Nat. Phys.* **13**, 369 (2016).
- [28] A. K. Geim and K. S. Novoselov, *Nat. Mater.* **6**, 183 (2007).
- [29] A. H. C. Neto, F. Guinea, N. M. R. Peres, K. S. Novoselov, and A. K. Geim, *Rev. Mod. Phys.* **81**, 109 (2009).
- [30] H. Zhu and F. Semperlotti, (2017), arXiv:1706.01536v1 [cond-mat.mtrl-sci].